



# **A new cosmic shear function: optimized E-/B-mode decomposition on a finite interval**

Liping Fu, Martin Kilbinger

## **► To cite this version:**

Liping Fu, Martin Kilbinger. A new cosmic shear function: optimized E-/B-mode decomposition on a finite interval. Monthly Notices of the Royal Astronomical Society, 2010, 401, pp.1264-1274. <10.1111/j.1365-2966.2009.15720.x>. <hal-03646188>

**HAL Id: hal-03646188**

**<https://hal.science/hal-03646188v1>**

Submitted on 22 May 2022

**HAL** is a multi-disciplinary open access archive for the deposit and dissemination of scientific research documents, whether they are published or not. The documents may come from teaching and research institutions in France or abroad, or from public or private research centers.

L'archive ouverte pluridisciplinaire **HAL**, est destinée au dépôt et à la diffusion de documents scientifiques de niveau recherche, publiés ou non, émanant des établissements d'enseignement et de recherche français ou étrangers, des laboratoires publics ou privés.



HAL Authorization

# A new cosmic shear function: optimized E-/B-mode decomposition on a finite interval

Liping Fu<sup>1,2★</sup> and Martin Kilbinger<sup>3</sup>

<sup>1</sup>INAF, Osservatorio Astronomico di Capodimonte, via Moiariello 16, 80131 Napoli, Italy

<sup>2</sup>Shanghai Key Lab for Astrophysics, Shanghai Normal University, Shanghai 200234, P. R. China

<sup>3</sup>Institut d'Astrophysique de Paris, 98bis boulevard Arago, F-75014 Paris, France

Accepted 2009 September 14. Received 2009 September 14; in original form 2009 July 3

## ABSTRACT

The decomposition of the cosmic shear field into E and B mode is an important diagnostic in weak gravitational lensing. However, commonly used techniques to perform this separation suffer from mode-mixing on very small or very large scales. We introduce a new E-/B-mode decomposition of the cosmic shear two-point correlation on a finite interval. This new statistic is optimized for cosmological applications, by maximizing the signal-to-noise ratio (S/N) and a figure of merit (FoM) based on the Fisher matrix of the cosmological parameters  $\Omega_m$  and  $\sigma_8$ .

We improve both S/N and FoM results substantially with respect to the recently introduced ring statistic, which also provides E-/B-mode separation on a finite angular range. The S/N (FoM) is larger by a factor of 3 (2) on angular scales between 1 and 220 arcmin. In addition, it yields better results than for the aperture-mass dispersion  $\langle M_{\text{ap}}^2 \rangle$ , with improvements of 20 per cent (10 per cent) for S/N (FoM). Our results depend on the survey parameters, most importantly on the covariance of the two-point shear correlation function. Although we assume parameters according to the CFHTLS-Wide survey, our method and optimization scheme can be applied easily to any given survey settings and observing parameters. Arbitrary quantities, with respect to which the E-/B-mode filter is optimized, can be defined, therefore generalizing the aim and context of the new shear statistic.

**Key words:** gravitational lensing – large-scale structure of Universe.

## 1 INTRODUCTION

Cosmic shear, the weak gravitational lensing effect induced on images of distant galaxies by the large-scale structure in the Universe, has become a standard tool for observational cosmology (see Schneider 2006; Hoekstra & Jain 2008; Munshi et al. 2008, for recent reviews). Large surveys have used cosmic shear to obtain measurements of the matter density  $\Omega_m$  and the density fluctuation amplitude  $\sigma_8$ . Recent constraints were obtained from ground-based surveys such as CFHTLS<sup>1</sup> (Benjamin et al. 2007; Fu et al. 2008) and GaBoDS<sup>2</sup> (Hettterscheidt et al. 2007). Space-based surveys like COSMOS<sup>3</sup> (Leauthaud et al. 2007; Massey et al. 2007) and parallel ACS data (Schrabback et al. 2007) advanced cosmic shear observations to very small angular scales. Cosmic shear has contributed to constraining dark energy (Jarvis et al. 2006; Kilbinger et al. 2009). It is considered to be one of the most promising methods to shed

light on to the origin of the recent accelerated expansion of the Universe (Albrecht et al. 2006; Peacock et al. 2006), and is a major science driver for many future surveys like KIDS, Pan-STARRS, DES, LSST, JDEM or Euclid.

One of the (few) diagnostics for cosmic shear analyses is the decomposition of the shear field into its E and B mode. Most commonly, the shear power spectrum or, equivalently, the shear correlation function, is split into the gradient (E) and curl (B) component (Crittenden et al. 2002; Schneider, Van Waerbeke & Mellier 2002). Gravitational lensing produces, to the first order, a curl-free shear field, and therefore the presence of a B mode is an indication of residual systematics in the point spread function (PSF) correction and shape measurement analysis. To obtain competitive constraints on cosmological parameters, in particular for dark-energy or beyond-standard physics, galaxy shapes have to be determined to subper centage precision. This requires excellent correction of PSF effects arising from the atmosphere, telescope and camera imperfections.

Apart from observational effects and measurement systematics, the cosmic shear signal can be severely contaminated by intrinsic correlations of galaxy orientation with other galaxies or their surrounding dark matter structures (Heavens, Réfrégier & Heymans 2000). This occurs for galaxies at the same redshift, e.g. which

★E-mail: fu@oacn.inaf.it

<sup>1</sup><http://www.cfht.hawaii.edu/Science/CFHTLS>

<sup>2</sup>[http://archive.eso.org/archive/adp/GaBoDS/DPS\\_stacked\\_images\\_v1.0](http://archive.eso.org/archive/adp/GaBoDS/DPS_stacked_images_v1.0)

<sup>3</sup><http://cosmos.astro.caltech.edu>

reside in the same dark halo (*intrinsic alignment*). It also affects galaxies at very different redshifts, where a background galaxy is lensed by matter surrounding a foreground galaxy, therefore inducing a *shape-shear-correlation* between the two galaxies. An E mode, as well as a B mode, arises from intrinsic alignment (Crittenden et al. 2002; Mackey, White & Kamionkowski 2002).

Standard methods to separate the E- and B-mode power spectra (or correlation functions) involve integrals up to arbitrary small or large angular scales (Schneider et al. 1998; Crittenden et al. 2002; Schneider et al. 2002). However, shear correlations can be observed only on a finite interval. Since the shear field is probed at galaxy positions, the smallest usable scale is given by the confusion limit for close galaxy pairs, which is typically several arcmin for ground-based surveys. The largest observed distance for current surveys is several degrees. These limits make the E-/B-mode separation imperfect, and a mixing of modes is induced at the 1–10 per cent level (Kilbinger, Schneider & Eifler 2006). To circumvent this shortcoming, a new second-order function, the so-called ‘ring statistic’, was introduced which permits a clear E-/B-mode separation on a finite interval (Schneider & Kilbinger 2007, hereafter SK07). In addition, the authors developed conditions for general filter functions necessary for an E-/B-mode decomposition for a finite angular range.

In this work, we present a method to find filter functions which fulfil the SK07 conditions. We devise a scheme which provides an optimized E-/B-mode decomposition on a finite interval. The optimization is performed with regard to cosmological applications of cosmic shear; the signal-to-noise ratio (S/N) and a Fisher matrix figure of merit are the quantities to be maximized. This paper is organized as follows. In Section 2, we briefly review the results from SK07 before we present our optimization method. Results for the S/N and the figure of merit (FoM) are shown in Section 3. We conclude the paper with a summary (Section 4) and an outlook (Section 5).

## 2 METHOD

### 2.1 E-and B-mode decomposition of the shear correlation function on a finite interval

We define the general second-order cosmic shear functions  $\mathcal{R}_E$  and  $\mathcal{R}_B$ ,

$$\begin{aligned}\mathcal{R}_E &= \frac{1}{2} \int_0^\infty d\vartheta \vartheta [T_+(\vartheta) \xi_+(\vartheta) + T_-(\vartheta) \xi_-(\vartheta)], \\ \mathcal{R}_B &= \frac{1}{2} \int_0^\infty d\vartheta \vartheta [T_+(\vartheta) \xi_+(\vartheta) - T_-(\vartheta) \xi_-(\vartheta)],\end{aligned}\quad (1)$$

as integrals over the shear two-point correlation functions  $\xi_+$  and  $\xi_-$  (e.g. Kaiser 1992) with arbitrary filter functions  $T_+$  and  $T_-$ . These expressions correspond to equation (39) from SK07, with an additional factor of 1/2 in our definition. In terms of the E- and B-mode power spectrum,  $P_E$  and  $P_B$ , respectively, the shear two-point correlation function is given as the following Hankel transforms (Schneider et al. 2002):

$$\begin{aligned}\xi_+(\vartheta) &= \int_0^\infty \frac{d\ell}{2\pi} J_0(\ell\vartheta) [P_E(\ell) + P_B(\ell)]; \\ \xi_-(\vartheta) &= \int_0^\infty \frac{d\ell}{2\pi} J_4(\ell\vartheta) [P_E(\ell) - P_B(\ell)],\end{aligned}\quad (2)$$

with  $J_\nu$  being the  $\nu$ th-order Bessel function of the first kind. Inserting equation (2) into equation (1) yields

$$\begin{aligned}\mathcal{R}_E &= \frac{1}{2} \int_0^\infty \frac{d\ell}{2\pi} \left\{ P_E(\ell) [\mathcal{W}_E(\ell) + \mathcal{W}_B(\ell)] \right. \\ &\quad \left. + P_B(\ell) [\mathcal{W}_E(\ell) - \mathcal{W}_B(\ell)] \right\},\end{aligned}\quad (3)$$

and an analogous expression for  $\mathcal{R}_B$ . The Hankel transforms of  $T_+$  and  $T_-$  are defined as

$$\mathcal{W}_{E,B}(\ell) = \int_0^\infty d\vartheta \vartheta T_{+,-}(\vartheta) J_{0,4}(\vartheta\ell). \quad (4)$$

To provide an E- and B-mode decomposition, in the sense that  $\mathcal{R}_E$  only depends on the E mode of the shear field and  $\mathcal{R}_B$  only on its B mode, the two Hankel transforms have to be identical,  $\mathcal{W}_E = \mathcal{W}_B$ . After some algebra, one finds that the following equivalent relations between the filter functions  $T_+$  and  $T_-$  must hold (Schneider et al. 2002):

$$T_+(\vartheta) = T_-(\vartheta) + 4 \int_\vartheta^\infty \frac{d\theta}{\theta^2} T_-(\theta) \left[ 1 - 3 \left( \frac{\vartheta}{\theta} \right)^2 \right], \quad (5)$$

$$T_-(\vartheta) = T_+(\vartheta) + 4 \int_0^\vartheta \frac{d\theta}{\theta^2} T_+(\theta) \left[ 1 - 3 \left( \frac{\theta}{\vartheta} \right)^2 \right]. \quad (6)$$

Therefore, for an arbitrary function  $T_+$ , a corresponding filter  $T_-$  can be derived from  $T_+$  to provide an E- and B-mode decomposition, and vice versa. In the absence of a B mode we have  $\mathcal{R}_B = 0$ , and  $\mathcal{R}_E$  can be obtained from  $\xi_+$  or  $\xi_-$  alone,

$$\mathcal{R}_E = \int_0^\infty d\vartheta \vartheta T_+(\vartheta) \xi_+(\vartheta) = \int_0^\infty d\vartheta \vartheta T_-(\vartheta) \xi_-(\vartheta). \quad (7)$$

We further require  $\mathcal{R}_E$  and  $\mathcal{R}_B$  to depend on the shear correlation given at angular scales  $\vartheta$  in a finite interval,  $0 < \vartheta_{\min} \leq \vartheta \leq \vartheta_{\max} < \infty$ . Thus, we demand  $T_-$  to have finite support  $[\vartheta_{\min}; \vartheta_{\max}]$  and  $T_+(\vartheta)$  to vanish for  $\vartheta < \vartheta_{\min}$ ; equation (5) then implies the following integral constraints on the filter function  $T_-$  (SK07):

$$\int_{\vartheta_{\min}}^{\vartheta_{\max}} \frac{d\vartheta}{\vartheta} T_-(\vartheta) = \int_{\vartheta_{\min}}^{\vartheta_{\max}} \frac{d\vartheta}{\vartheta^3} T_-(\vartheta) = 0. \quad (8)$$

In addition, it follows that  $T_+(\vartheta) = 0$  for  $\vartheta > \vartheta_{\max}$ . Using the finite support of  $T_+$  in equation (6), we get integral constraints for  $T_+$ :

$$\int_{\vartheta_{\min}}^{\vartheta_{\max}} d\vartheta \vartheta T_+(\vartheta) = \int_{\vartheta_{\min}}^{\vartheta_{\max}} d\vartheta \vartheta^3 T_+(\vartheta) = 0. \quad (9)$$

Then,  $\mathcal{R}_E$  and  $\mathcal{R}_B$  are functions of the two angular scales  $\vartheta_{\min}$  and  $\vartheta_{\max}$ . We will discuss the scale-dependence in more detail in Section 2.6.

SK07 constructed a set of functions,  $Z_+$ ,  $Z_-$  in their notation, which satisfy equations (8) and (9). Those functions were motivated from a geometrical ansatz, by considering two concentric, non-overlapping rings. If the shear correlation is calculated from galaxy pairs of which one galaxy lies in the inner ring and the other galaxy in the outer ring, the E-/B-mode decomposition on a finite interval is guaranteed by construction. The form of the function  $Z_+$  originated in a specific choice of the weight profile over the two rings. The relation between  $T_\pm$  and  $Z_\pm$  is

$$T_\pm(\vartheta) = \vartheta^{-2} Z_\pm(\vartheta/\vartheta_{\max}). \quad (10)$$

Note that in SK07 the analogous integrals to equation (1) using  $Z_\pm$  are carried out over the integration variable  $\vartheta/\vartheta_{\max}$  and extend from  $\vartheta_{\min}/\vartheta_{\max}$  to 1. The shear second-order functions corresponding to equation (1) are denoted as  $\langle \mathcal{R} \rangle_E$  and  $\langle \mathcal{R} \rangle_B$ , respectively.

There are infinitely many functions which fulfil the above integral constraints. Their choice can, of course, be detached from the geometrical considerations of the ‘ring statistic’. In this paper, we define a general filter function which we will optimize regarding some specific criterion. This criterion will be related to the cosmological information output from a cosmic shear survey. We will use two cases, the S/N and the Fisher matrix of cosmological parameters. The results are presented in Section 3.

## 2.2 Parametrization of the filter function

For the optimization problem, we focus on  $T_+$  since  $T_-$  can be derived from  $T_+$  (equation 6). First, we remap  $T_+$  to the interval  $[-1; +1]$  by defining

$$\tilde{T}_+(x) = T_+(Ax + B) = T_+(\vartheta) \quad \text{for } x \in [-1; 1];$$

$$A = (\vartheta_{\max} - \vartheta_{\min})/2; \quad B = (\vartheta_{\max} + \vartheta_{\min})/2.$$

With that the two integral constraints (equation 9) become

$$\int_{-1}^{+1} dx (x + R) \tilde{T}_+(x) = \int_{-1}^{+1} dx (x + R)^3 \tilde{T}_+(x) = 0, \quad (12)$$

where we have defined the ratio  $R$  as

$$R = \frac{B}{A} = \frac{1 + \eta}{1 - \eta}; \quad \eta = \frac{\vartheta_{\min}}{\vartheta_{\max}}. \quad (13)$$

Next, we decompose  $\tilde{T}_+$  into a finite sum of orthogonal polynomials:

$$\tilde{T}_+(x) = \sum_{n=0}^{N-1} a_n C_n(x). \quad (14)$$

This representation allows us to find an optimal filter function by varying the coefficients  $a_n$  (Section 2.7). The polynomials  $C_n$  can be chosen freely; we use Chebyshev polynomials of the second kind,

$$U_n(x) = \frac{\sin[(n+1)\arccos x]}{\sin(\arccos x)}. \quad (15)$$

The optimization process is then performed by varying the coefficients  $a_n$ ; this is described in detail in Section 2.7.

Apart from the integral constraints (equation 9), one could require  $T_+$  to be zero at the interval boundaries,

$$\text{Continuity: } T_+(\vartheta_{\max}) = T_+(\vartheta_{\min}) = 0. \quad (16)$$

Additional constraints could be added, for example differentiability at the boundaries. We will discuss their effects on the results in Section 3.1.

## 2.3 Satisfying the constraints

In general, the function  $T_+$ , or equivalently  $\tilde{T}_+$ , is constrained by  $K \geq 2$  equations in the form  $F_m[\tilde{T}_+] = 0$ ,  $m = 0 \dots K-1$ . If the functionals  $F_m$  are linear in  $\tilde{T}_+$ , applying equation (14) leads to

$$\sum_{n=0}^{N-1} f_{mn} a_n = 0; \quad f_{mn} := F_m[C_n]. \quad (17)$$

The matrix element  $f_{mn}$  is the  $m$ th constraint applied to the orthogonal polynomial of order  $n$ . For example, taking the first constraint in equation (12), we get

$$f_{0n} = \int_{-1}^{+1} dx (x + R) C_n(x), \quad (18)$$

which can be integrated analytically. The other matrix elements  $f_{mn}$  are obtained analogously.

$K$  constraints fix  $K$  coefficients of the decomposition (equation 14), the remaining  $N - K$  coefficients can be chosen arbitrarily. We use the highest  $N - K$  coefficients as free parameters ( $n = K \dots N - 1$ ) and fix the first  $K$  coefficients ( $n = 0 \dots K - 1$ ) as follows. Defining

$$s_m = - \sum_{n=K}^{N-1} f_{mn} a_n; \quad m = 0 \dots K - 1, \quad (19)$$

equation (17) can then be written as

$$\sum_{n=0}^{K-1} f_{mn} a_n = s_m; \quad m = 0 \dots K - 1. \quad (20)$$

This  $(K \times K)$ -matrix equation is solved for the first  $K$  coefficients  $a_n$  ( $n = 0 \dots K - 1$ ) by inverting the square (sub)matrix  $(f_{mn})_{m,n < K}$  on the left-hand side of the above equation. If the constraints are chosen such that they are linearly independent (which is this case), this matrix equation has a unique, non-trivial solution.

In addition to the  $K$  constraints, we impose an integral normalization of the filter function given by the  $L^2$ -norm:

$$\|\tilde{T}_+\|_2^2 = \int_{-1}^1 dx w(x) \tilde{T}_+^2(x) = 1, \quad (21)$$

where  $w$  is the corresponding weight of the polynomial family,  $w(x) = (1 - x^2)^{1/2}$  in the case of second-kind Chebyshev polynomials. This normalization does not affect the constraints which are independent of a multiplication of all  $a_n$  with a common factor. Note also that the quantities which we will optimize in Section 3 do not depend on the normalization.

## 2.4 Calculation of $T_-$ from $T_+$

To obtain the function  $\tilde{T}_- := T_-(Ax + B)$ , we transform equation (6) to

$$\tilde{T}_-(x) = \tilde{T}_+(x) + 4 \int_{-1}^x dx' \tilde{T}_+(x') \frac{x' + R}{(x + R)^2} \left[ 1 - 3 \left( \frac{x' + R}{x + R} \right)^2 \right];$$

$$x = -1 \dots 1, \quad (22)$$

which can be written as

$$\tilde{T}_-(x) = \sum_{n=0}^{N-1} a_n [C_n(x) + \alpha_n(x)]; \quad (23)$$

$$\alpha_n(x) = 4 \int_{-1}^x dx' C_n(x') \frac{x' + R}{(x + R)^2} \left[ 1 - 3 \left( \frac{x' + R}{x + R} \right)^2 \right], \quad (24)$$

inserting the decomposition (equation 14). We define

$$F_n^{(v)}(x) = \int_{-1}^x dx' (x')^v C_n(x'); \quad v = 0, 1, 2, 3, \quad (25)$$

and write equation (24) as

$$\alpha_n(x) = \frac{4}{3} r [R(r - R)F_n^{(0)} + (1 - 2rR - rR^2)F_n^{(1)} - rR(R + 2)F_n^{(2)} - rF_n^{(3)}];$$

$$r = \frac{3}{(x + R)^2}, \quad (26)$$

where we dropped the argument  $x$  from  $F_n^{(v)}$  and  $r$ . The integral (equation 25) for  $v = 0$  and  $C_n = U_n$  is

$$F_n^{(0)}(x) = \begin{cases} \frac{(-1)^n + x T_n(x) - (1 - x^2) U_{n-1}(x)}{n+1} & (n \neq -1) \\ 0 & (n = -1) \end{cases}, \quad (27)$$

where  $T_n$  is  $n$ th-order Chebyshev polynomial of the first kind,

$$T_n(x) = \cos(n \arccos x). \quad (28)$$

By using the recurrence relation of the Chebyshev polynomials, we obtain the other functions,

$$\begin{aligned} F_n^{(1)} &= \frac{1}{2} [F_{n+1}^{(0)} + F_{n-1}^{(0)}]; \\ F_n^{(2)} &= \frac{1}{4} [F_{n+2}^{(0)} + 2F_n^{(0)} + F_{n-2}^{(0)}]; \\ F_n^{(3)} &= \frac{1}{8} [F_{n+3}^{(0)} + 3F_{n+1}^{(0)} + 3F_{n-1}^{(0)} + F_{n-3}^{(0)}]. \end{aligned} \quad (29)$$

Note that equation (27) is valid for integer  $n$ , since the expressions for the orthogonal polynomials are well defined for negative  $n$ .

With that, it can be readily checked whether the coefficients  $a_n$  obtained with the method described in Section 2.3 and the resulting filter functions  $\tilde{T}_\pm$  indeed provide an E-/B-mode decomposition, by verifying that the B-mode  $\mathcal{R}_B$  (equation 1) is zero. In Section 3.6, we discuss numerical issues when calculating the B mode.

## 2.5 Relation to the lensing power spectrum

Equation (3) shows the relation of  $\mathcal{R}_E$  to the power spectrum. Assuming a pure E mode, this equation reads

$$\mathcal{R}_E = \frac{1}{2\pi} \int_0^\infty d\ell \ell P_E(\ell) \mathcal{W}_E(\ell), \quad (30)$$

where the Fourier-space filter function  $\mathcal{W}_E$  can be written as

$$\mathcal{W}_E(\ell, \vartheta_{\min}, \vartheta_{\max}) = \sum_{n=0}^{N-1} a_n \mathcal{W}_n(\ell, \vartheta_{\min}, \vartheta_{\max}), \quad (31)$$

$$\mathcal{W}_n(\ell, \vartheta_{\min}, \vartheta_{\max}) = \int_{\vartheta_{\min}}^{\vartheta_{\max}} d\vartheta \vartheta C_n[(\vartheta - B)/A] J_0(\vartheta \ell), \quad (32)$$

with  $A$  and  $B$  given in equation (11). Analogously,  $\mathcal{R}_B$  can be written in terms of the B-mode power spectrum  $P_B$ :

$$\mathcal{R}_B = \frac{1}{2\pi} \int_0^\infty d\ell \ell P_B(\ell) \mathcal{W}_B(\ell, \vartheta_{\min}, \vartheta_{\max}), \quad (33)$$

with  $\mathcal{W}_E = \mathcal{W}_B$  (see Section 2.1).

Unfortunately, there is no simple analytical expression of equation (32), which would be desirable to calculate equation (30) using a fast Hankel transform (FHT; Hamilton 2000). For the moment, the most efficient method to calculate  $\mathcal{R}_E$  from a model power spectrum is to obtain  $\xi_+$  from  $P_E$  by FHT and to integrate it via equation (7) which is fast since in our case  $T_+$  is a rather low-order polynomial, as we will see later.

## 2.6 Angular-scale-dependence

The two constraints (equation 9) depend on the ratio of angular scales  $\eta = \vartheta_{\min}/\vartheta_{\max}$ . A filter function  $\tilde{T}_+$  with given coefficients  $a_n$  satisfying those constraints does not in general fulfil the same

constraints for a different  $\eta$ . This therefore causes the inconvenience of having a different filter function for each angular scale.

It should be noted that although formally  $\mathcal{R}_E$  is a function of two angular scales, the information about cosmology and large-scale structure is captured by a single parameter, let us call it  $\lambda$ . This is because the large-scale matter power spectrum, of which  $\mathcal{R}_E$  is a logarithmic convolution (Section 2.5), only depends on a single scalar. We therefore expect a large covariance between many pairs  $(\vartheta_{\min}, \vartheta_{\max})$ . Although there are infinitely many mappings  $(\vartheta_{\min}, \vartheta_{\max}) \rightarrow \lambda$ , two ways to handle the scale-dependence seem to be suitable. (1) Leaving one scale constant, and varying the other scale, e.g.,  $\vartheta_{\min} = \text{const.}$ ,  $\lambda = \vartheta_{\max}$ . (2) Leaving the ratio of both scales constant,  $\lambda = \eta$ . We will pursue both ways in this paper.

### 2.6.1 Fixed minimum scale, $\vartheta_{\min} = \text{const.}$

The first mapping introduced above offers a rather efficient sampling of the shear field.  $\vartheta_{\min}$  can be fixed to the smallest observable distance  $\vartheta_{\min,0}$  for which shear correlation data are measured. This is given by the smallest separation for which galaxies do not blend, to allow for reliably measured shapes. It provides the largest range of angular scales accessible for a given  $\vartheta_{\max}$ : the upper limit  $\vartheta_{\max}$  can be varied between  $\vartheta_{\min}$  and the maximum observed scale given by the data.

### 2.6.2 Fixed ratio, $\eta = \vartheta_{\min}/\vartheta_{\max} = \text{const.}$

The second mapping has the advantage that a single filter function can satisfy the constraints (equation 9) for all scales. This makes it more convenient to combine different scales, e.g. to obtain the Fisher matrix, and might result in a universal optimal filter function. The efficiency with respect to keeping  $\vartheta_{\min}$  constant is however reduced: a large ratio  $\eta$ , for which  $\vartheta_{\min}$  and  $\vartheta_{\max}$  are close, samples only a small angular interval, resulting in a small S/N. A small  $\eta$  on the other hand means that we cannot go to very small scales with  $\vartheta_{\max}$ : because of the minimum observable galaxy separation  $\vartheta_{\min,0}$ , the smallest  $\vartheta_{\max}$  is  $\min(\vartheta_{\max}) = \vartheta_{\min,0}/\eta$ .

In both cases, we will use  $\vartheta_{\max}$  as the argument of  $\mathcal{R}_E$  and denote it with the symbol  $\Psi$ , as in SK07.

In Appendix A, we introduce a simple generalization of this scheme to obtain an optimized function  $\tilde{T}_+$  which fulfils the integral constraints (equation 9) for all pairs  $(\vartheta_{\min}, \vartheta_{\max})$ . However, the corresponding S/N is significantly lower than with the method used here, which was presented in Section 2.3. We therefore do not consider this option further.

A remark about the analogy to the aperture-mass dispersion  $\langle M_{\text{ap}}^2 \rangle$  is appropriate here.  $\langle M_{\text{ap}}^2 \rangle$  is obtained from the correlation function in a similar way as  $\mathcal{R}_E$  in equation (1), with integration range between zero and twice the aperture radius. Its filter function depends on the two scales  $\vartheta$  (the integration variable) and  $\theta$  (the aperture radius). For different  $\theta$  one could define a different filter function. For convenience however, widely used filters are functions of the ratio  $\vartheta/\theta$ , and therefore one functional form provides an E-/B-mode separation for all radii simultaneously.

## 2.7 Optimization

The maximization of a quantity  $Q$ , to be defined in the next section as S/N and Fisher matrix FoM, is done as follows. For a given polynomial of order  $N$ , number of constraints  $K \geq 2$ , we perform the maximum search of  $Q$  using the conjugate-gradient method

**Table 1.** Overview of quantities kept fixed when varying the scales  $\Psi$ , and the corresponding method to determine the starting point for subsequent scales.

$Q$	Fixed quantity	Starting point for subsequent scales
S/N	$\vartheta_{\min} = \text{const.}$	Previous maximum function, $\tilde{T}_+$
S/N	$\eta = \text{const.}$	Previous maximum coefficients $a_n$
FoM	$\eta = \text{const.}$	Previous maximum coefficients $a_n$

(Press et al. 1992) in the space of free coefficients  $a_K, \dots, a_{N-1}$ . At each step, we calculate  $s_m$  (equation 19) and invert equation (20) to get the first  $K$  coefficients  $a_0, \dots, a_{K-1}$ ; from there we compute  $\tilde{T}_+$  (equation 14) and  $\mathcal{R}_E$  (equation 7).

We limit each of the coefficients  $a_K, \dots, a_{N-1}$  to the box  $[-10; 10]$ . In some cases, the maximum-search fails, in particular if the polynomial order is high. The algorithm might run into a local maximum or hit the parameter boundary. To reduce the failure rate, we proceed as follows.

If a maximum is found close to the parameter boundary, we discard it and redo the maximization with larger box size for a different starting point. To initialize the maximization for the first of a range of angular scales, we draw a number of random points, on the order of 100, and start the maximization with the point providing the largest  $Q$ .

For subsequent angular scales, we use the information about the previous maximum to start the next optimization. If the ratio  $\eta = \vartheta_{\min}/\vartheta_{\max}$  is kept constant when increasing  $\vartheta_{\max} = \Psi$ , we use the previous maximum coefficients  $a_n$  as new starting value for the maximization process. This renders the search for the maximum point more efficient and more stable, since for small changes in  $\Psi$  the maximum will be close in  $a$ -space.

For constant minimum scale  $\vartheta_{\min}$ , we devise a different strategy. It can be shown that in this case,  $Q$  is monotonously increasing with  $\Psi$ : let  $T_+^{(i)}$  be the function for scale  $\Psi_i$  which maximizes  $Q(\Psi_i)$ . For the subsequent scale  $\Psi_{i+1} > \Psi_i$ , define the function  $\tilde{T}_+(\Psi) = T_+^{(i)}(\Psi)$  for  $\Psi < \Psi_i$ , and  $\tilde{T}_+(\Psi) = 0$  otherwise. By construction, the resulting  $Q$  for scale  $\Psi_{i+1}$  is the same as for  $\Psi_i$ ,  $Q(\Psi_{i+1}) = Q(\Psi_i)$ . Therefore, we choose as new starting point for scale  $\Psi_{i+1}$  the coefficients resulting from the decomposition of the function  $\tilde{T}_+(\Psi)$ . This assures the subsequent maximum  $Q(\Psi_{i+1})$  found by the search algorithm to be larger or equal to the previous one, at least in the limit of large  $N$ . In practice, however, due to the finite order  $N$ , the orthogonal polynomials are not a good representation of  $\tilde{T}_+$  for  $\Psi > \Psi_i$  where it is zero, and the resulting  $Q$  can actually decrease with increasing scale.

We summarize the combinations of  $Q$ , the angular dependencies and the choice of the starting point for subsequent scales in Table 1.

### 3 RESULTS

In this section, we define  $Q$  according to S/N and a Fisher-matrix FoM, respectively, which we maximize to find the corresponding optimized filter function  $\tilde{T}_+$ . Before that, we comment on our choice of  $K$  and  $N$ , the number of constraints and polynomial order, respectively.

#### 3.1 Number of constraints and polynomial order

We choose the minimum number of constraints  $K = 2$  necessary for a finite-interval E- and B-mode decomposition, corresponding to the two integral constraints (equation 9). Adding the two continuity

constraints (equation 16) resulted in significantly lower values of  $Q$ . Some of the resulting functions  $\tilde{T}_\pm$  showed strong variations and narrow peaks for  $|x|$  near unity. This indicates that the continuity constraint is not very ‘natural’ but represents a strong restriction on the optimized filter functions. The price that has to be paid for continuity is then a function which fluctuates strongly, which may be problematic when applied to noisy data.

Larger values of  $N$  improved  $Q$  to some extent but at the same time increased the occurrence of local maxima found by the search algorithm, reducing stability and reproducibility of the results. The functions  $\tilde{T}_\pm$  sometimes showed a high number of oscillations. A good choice for the polynomial of order  $N$  was found to be six, equivalent to four free parameters  $a_n$  for  $K = 2$ . A lower  $N$  resulted in significantly smaller  $Q$ .

For the remainder of this paper, we therefore choose  $N = 6$ ,  $K = 2$ , if not indicated otherwise.

#### 3.2 Shear covariance and cosmology

For the optimization process, we rely on a model shear correlation function and covariance. The fiducial cosmology for our model is a flat  $\Lambda$  cold dark matter (CDM) Universe with  $\Omega_m = 0.25$ ,  $\Omega_b = 0.044$ ,  $h = 0.7$  and  $\sigma_8 = 0.8$ . We use the non-linear fitting formula of Smith et al. (2003) together with the Eisenstein & Hu (1998) transfer function for the matter power spectrum. The redshift distribution of source galaxies is the best-fitting model of Fu et al. (2008) which has a mean redshift of 0.95.

We use the covariance matrix  $C_{++}$  of the shear correlation function  $\xi_+$  from Fu et al. (2008), corresponding to the third data release of CFHTLS-Wide. This includes ellipticity noise and cosmic variance as well as the residual B mode added in quadrature. The Gaussian part of the covariance was calculated using the method from Kilbinger & Schneider (2004). Non-Gaussian corrections on small scale were applied according to Semboloni et al. (2007).

The  $\mathcal{R}_E$ -covariance matrix,  $\langle \mathcal{R}_E^2 \rangle$ , is an integral over  $C_{++}$ :

$$\langle \mathcal{R}_E^2(\Psi_1, \Psi_2) \rangle = \int_{\vartheta_{\min,1}}^{\Psi_1} d\vartheta \vartheta T_+(\vartheta) \int_{\vartheta_{\min,2}}^{\Psi_2} d\vartheta' \vartheta' T_+(\vartheta') C_{++}(\vartheta, \vartheta'). \quad (34)$$

We use the two upper scale limits  $\Psi_1$  and  $\Psi_2$  as arguments of  $\langle \mathcal{R}_E^2 \rangle$ ; it also depends on the two lower scale limits  $\vartheta_{\min,1}$  and  $\vartheta_{\min,2}$ .

#### 3.3 Signal-to-noise ratio

The first criterion for which we optimize the filter function is the S/N:

$$S/N(\Psi) = \frac{\mathcal{R}_E(\Psi)}{\langle \mathcal{R}_E^2(\Psi, \Psi) \rangle^{1/2}}. \quad (35)$$

The variance  $\langle \mathcal{R}_E^2(\Psi, \Psi) \rangle$  is the diagonal of equation (34). As mentioned before, the S/N does not depend on the normalization of  $\tilde{T}_+$  (equation 21).

##### 3.3.1 Signal-to-noise for fixed $\vartheta_{\min}$

The S/N is calculated as a function of  $\Psi = \vartheta_{\max}$ , keeping  $\vartheta_{\min}$  constant. We choose  $\vartheta_{\min} = 0.2$  arcmin which is a typical (albeit conservative) lower limit where galaxies from ground-based data can be well separated. For each scale  $\Psi$ , we obtain an optimized filter function  $T_+$ , as discussed in Section 2.7 (see Table 1).

As can be seen in the left-hand panel of Fig. 1 the optimal filter function with  $N = 6$  and  $K = 2$  results in a much higher S/N than

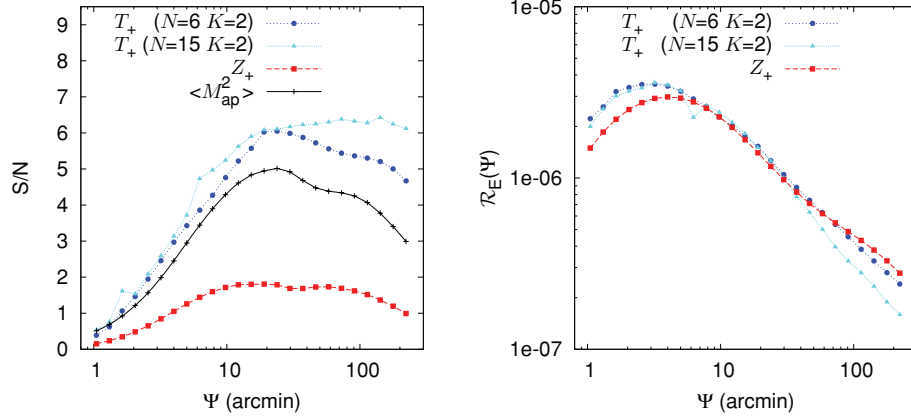


**Figure 1.** Left-hand panel: S/N for fixed  $\vartheta_{\min} = 0.2$  arcmin, as functions of the maximum scale  $\Psi$ . The blue curve with circles and the cyan with triangles correspond to polynomial of order  $N = 6$  and  $15$ , respectively. The red curve with squares shows the filter function from SK07. The black curve with crosses corresponds to the aperture-mass  $\langle M_{\text{ap}}^2 \rangle$  with  $\Psi$  being equal to the aperture diameter. Right-hand panel: the comparison of  $\mathcal{R}_E$  obtained from the optimized function  $T_+$  with polynomial of orders  $N = 6$  and  $15$ .

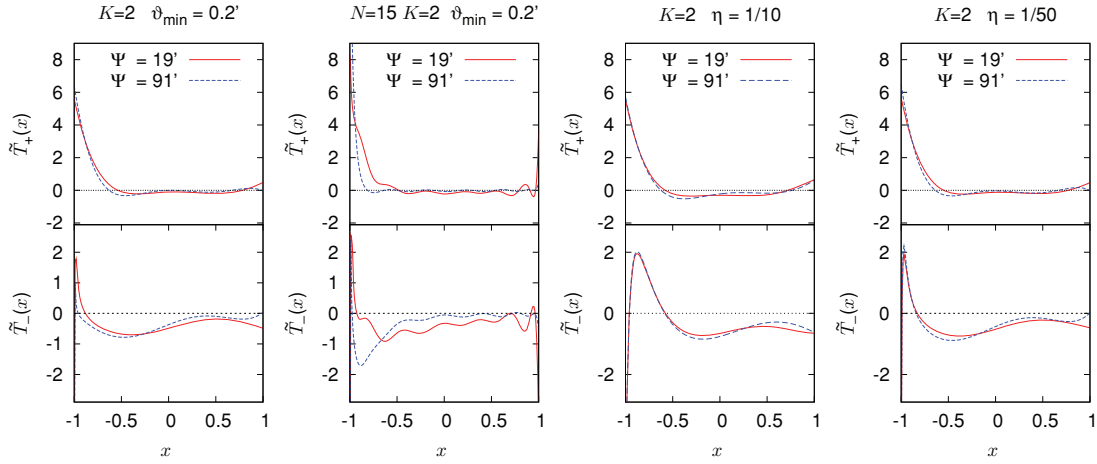


**Figure 2.** The normalized functions  $\tilde{T}_+$  and  $\tilde{T}_-$  optimized for S/N at scales  $\Psi = 19$  and  $91$  arcmin, respectively. Left two panels:  $\tilde{T}_+$  decomposed into polynomials of order  $N = 6$  and  $15$ , respectively, for fixed  $\vartheta_{\min} = 0.2$  arcmin. Right two panels: the comparison of fixed  $\eta = 1/10$  and  $1/50$  in the case of polynomials of order  $N = 6$ .

for original ring statistic function  $\langle \mathcal{R}\mathcal{R} \rangle_E$ , using the filter function  $Z_+$  from SK07. The new filter is superior to the aperture-mass dispersion. Note that we plot S/N for  $\langle M_{\text{ap}}^2 \rangle$  as a function of the aperture diameter instead of the radius, to have the same maximum shear correlation scale  $\Psi$  as for  $\mathcal{R}_E$ .

Although the optimal S/N is expected to be monotonic as a function of  $\Psi$ , this is clearly not the case. However, when increasing the polynomial of order  $N$  to  $15$ , the S/N is nearly constant for  $\Psi > 19$  arcmin and larger than for  $N = 6$  (see Fig. 1). As a drawback, the S/N curve for  $N = 15$  is less smooth due to the difficulty of finding the global maximum. We did, in general, not find significantly larger values for S/N with  $N$  larger than  $15$ .

The similar shape of S/N for the different cases  $\mathcal{R}_E$ ,  $\langle M_{\text{ap}}^2 \rangle$  and  $\langle \mathcal{R}\mathcal{R} \rangle_E$  is an imprint of the covariance structure of the shear correlation function. The shape is modified stronger for high  $N$ , where the peak at around  $20$  arcmin disappears.

The shear function  $\mathcal{R}_E$  is plotted in the right-hand panel of Fig. 1. It has a similar shape as  $\langle \mathcal{R}\mathcal{R} \rangle_E$  from SK07, and also as  $\langle M_{\text{ap}}^2 \rangle$ . This is reflecting the fact that all functions correspond to narrow filters and are bandpass convolution of the power spectrum.

The normalized optimal filter functions for two angular scales are shown in the left two panels of Fig. 2. The similarity of the functions for different scales shows the relatively weak dependence of the filter shape on angular scale.

### 3.3.2 Signal-to-noise for fixed $\eta$

Instead of fixing  $\vartheta_{\min}$ , we now leave  $\eta$  constant and change  $\vartheta_{\min}$  along with  $\Psi$ . The S/N increases with decreasing  $\eta$  (left-hand panel of Fig. 3). This is not surprising since a larger  $\eta$  means a smaller range of angular scales. For  $\eta = 1/50$ , the optimal S/N exceeds the one using the aperture-mass dispersion. The optimal filter functions have similar shape to the previous case of a fixed  $\vartheta_{\min}$  (see the right two panels of Fig. 2). We use the previous maximum coefficients  $a_n$  as starting point for subsequent scales as discussed in Section 2.7 (see Table 1). Unlike in the previous case of fixed  $\vartheta_{\min}$ , we do not expect S/N to be monotonous as a function of  $\Psi$ , because  $\vartheta_{\min}$  increases with  $\Psi$ .

Since  $\eta$  is constant, each filter function provides a valid E/B-mode decomposition for any given scale. We use the filter optimized

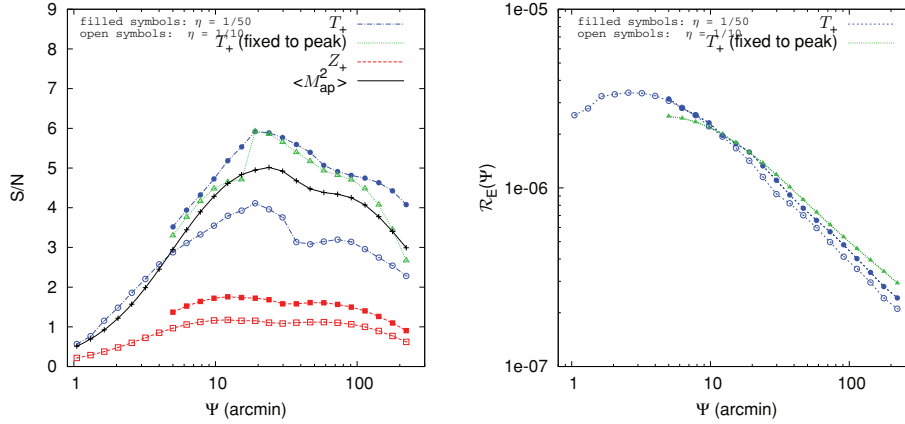


**Figure 3.** Left-hand panel: S/N as a function of  $\Psi$ , for fixed values of  $\eta$  with  $N = 6$  and  $K = 2$ . The blue curves correspond to the optimized function  $\tilde{T}_+$ . The green curve is obtained by applying the optimal function  $T_+$  of  $\Psi = 19$  arcmin to all scales, instead of optimizing each time separately, as done for the blue lines. The red curves show the filter function  $Z_+$  from SK07. The black curve with crosses corresponds to the aperture mass with aperture diameter  $\vartheta_{\max}$ . Filled and open symbols represent  $\eta = 1/50$  and  $1/10$ , respectively. Right-hand panel:  $\mathcal{R}_E$  for fixed values of  $\eta$  of  $1/10$  (open circles) and  $1/50$  (filled). For the green line (with filled triangles), the optimal function  $\tilde{T}_+$  for  $\Psi = 19$  arcmin was used on all scales, instead of optimizing each time separately as for the blue lines.

**Table 2.** Coefficients  $a_n$  of the optimized function  $\tilde{T}_+$  for (1) S/N,  $\Psi = 19$  arcmin,  $\eta = 1/50$ ; (2) FoM,  $\Psi_{\max} = 222$  arcmin,  $\eta = 1/10$ ; (3) FoM,  $\Psi_{\max} = 222$  arcmin,  $\eta = 1/50$ .

$n$	S/N( $\Psi = 19$ arcmin)	FoM ( $\Psi = 222$ arcmin)	
	$a_n$ ( $\eta = 1/50$ )	$a_n$ ( $\eta = 1/10$ )	$a_n$ ( $\eta = 1/50$ )
0	0.1197730890	0.009877788826	0.1239456383
1	-0.3881211865	0.1061397843	-0.3881431858
2	0.5212557875	-0.4300211814	0.5579593467
3	-0.3440507036	0.5451016406	-0.3679282338
4	0.2761305382	-0.3372272549	0.1540941993
5	-0.07286690971	0.1716983151	0.01293361618

for  $\Psi = 19$  arcmin, where the highest S/N occurs, and apply it to the other scales (see the green curve with triangles in the left-hand panel of Fig. 3). As expected, the S/N for scales  $\Psi \neq 19$  arcmin is lower than in the previous case, where the optimization was done for each scale individually. The difference, however, is not large and this case of fixed  $\eta$  shows a S/N which is mostly larger than the aperture-mass dispersion.

The shear function  $\mathcal{R}_E$  is plotted in the right-hand panel of Fig. 3; it is very similar in shape as in the case of fixed  $\vartheta_{\min}$  (Section 3.3.1). Table 2 shows the polynomial coefficients of the corresponding filter function  $\tilde{T}_+$ .

### 3.4 Fisher matrix

To optimize the filter function, we take now the alternative approach of minimizing the errors on cosmological parameters from our new second-order shear statistic. To that end, we use the Fisher matrix  $F$ , given by

$$F_{\alpha\beta} = \sum_{ij} \langle \mathcal{R}_E^2(\Psi_i, \Psi_j) \rangle^{-1} \frac{\partial \mathcal{R}_E(\Psi_i)}{\partial p_\alpha} \frac{\partial \mathcal{R}_E(\Psi_j)}{\partial p_\beta}. \quad (36)$$

The cosmological parameters are comprised in the vector  $\mathbf{p}$ . As in the case of the S/N, the Fisher matrix is independent of the normalization of the filter function  $\tilde{T}_+$ .

The quantity  $Q$  to be maximized is the inverse area of the error ellipsoid in parameter space, given by the Fisher matrix. In two

dimensions, this FoM (Albrecht et al. 2006) is

$$\text{FoM}^{-1} = \pi (\sigma_{11}\sigma_{22} - \sigma_{12}^2)^{1/2}; \quad \sigma_{ij}^2 = (F^{-1})_{ij}. \quad (37)$$

Eifler, Schneider & Krause (2009) used the quadrupole moment determinant  $q$  of the likelihood function to quantify the size of the parameter confidence region. In case of a Gaussian likelihood (which correspond to our Fisher matrix approximation) in two dimensions, the relation  $\text{FoM}^{-1} = \pi q$  holds.

We keep  $\eta$  constant, allowing for a single filter function  $\tilde{T}_+$  to provide the E- and B-mode decomposition for each scale  $\Psi$  in equation (36), and also for the covariance matrix. This requirement is not a necessity since the covariance between scales can be easily generalized to different filter functions. However, we choose this approach for simplicity. The cosmological parameters we consider are  $\Omega_m$  and  $\sigma_8$ .

In Fig. 4, we compare the FoM for the optimized filter function and the aperture-mass dispersion. For a given maximum scale  $\Psi_{\max}$ , we vary  $\Psi_i$  in equation (36) between 4.0 arcmin and  $\Psi_{\max}$ . With  $\eta = 1/50$ , the minimum angular scale is  $\min(\vartheta_{\min}) = 4.8$  arcsec. For  $\eta = 1/10$ , we use the same angular scales, starting with 4.0 arcmin, for consistency with the case  $\eta = 1/50$ . Alternatively, by using the same minimum angular scale of 4.8 arcsec, the smallest  $\Psi$  can be in principle as small as  $4.8 \text{ arcsec} / \eta = 0.8$  arcmin. This addition of small scales results in a higher FoM which is comparable to the one for  $\langle M_{\text{ap}}^2 \rangle$ .

We choose the same range of scales for the aperture-mass dispersion, i.e. we vary the aperture diameter between 4.0 arcmin and  $\Psi_{\max}$ . Note that although the minimum angular scale is theoretically zero, in practice we are limited by the smallest scale for which the  $\xi_+$ -covariance matrix is calculated which is 3 arcsec in our case.

The normalized optimal filter functions  $\tilde{T}_\pm$  are shown in Fig. 5. They have a similar shape as the functions optimized for S/N (see Fig. 2). Table 2 shows the corresponding polynomial coefficients.

### 3.5 The covariance of $\mathcal{R}_E$

We calculate the covariance matrix  $C$  of  $\mathcal{R}_E$  using the optimal filter function from the FoM maximization at the largest scale  $\Psi_{\max} = 222$  arcmin, for a constant  $\eta = 1/50$  (see Section 3.4). As can be seen in Fig. 6, the covariance is diagonally dominated, similar to



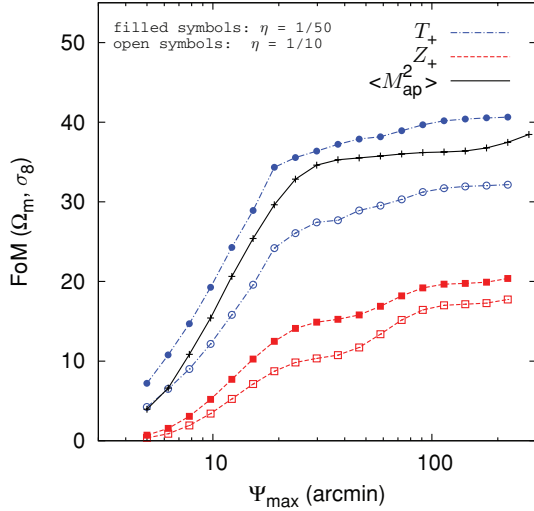


**Figure 4.** FoM (equation 37) for the optimized filter function  $T_+$  with  $\eta = 1/10$  and  $\eta = 1/50$  (blue curves). The red curves show the FoM for the filter function  $Z_+$  from SK07. The black curve with crosses corresponds to the aperture mass with aperture diameter  $\vartheta_{\max}$ . Filled and open symbols represent  $\eta = 1/50$  and  $1/10$ , respectively.

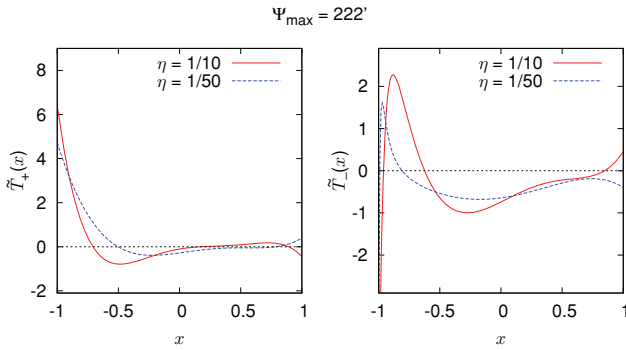


**Figure 5.** The normalized functions  $\tilde{T}_+$  and  $\tilde{T}_-$ , optimized for the Fisher matrix FoM (equation 37) with  $\Psi_{\max} = 222$  arcmin. Two cases,  $\eta = 1/10$  and  $1/50$ , are shown.

the one of the aperture-mass dispersion. The degree of correlation is seen more clearly by regarding the correlation matrix

$$r(\Psi_1, \Psi_2) = \frac{\langle \mathcal{R}_E^2(\Psi_1, \Psi_2) \rangle}{\langle \mathcal{R}_E^2(\Psi_1, \Psi_1) \rangle \langle \mathcal{R}_E^2(\Psi_2, \Psi_2) \rangle}, \quad (38)$$

see the right-hand panels of Fig. 6. To quantify the correlation length, we compute the following function:

$$\tau(x) = \langle r(\Psi, x\Psi) \rangle_\Psi, \quad (39)$$

which is the correlation between two scales separated by the multiplicative factor  $x$ , averaged over all  $\Psi$ . This function is shown in Fig. 7. Since the lines of equal  $r$  are mainly parallel to the diagonal, the scatter is relatively small. The correlation of  $\mathcal{R}_E$  drops off faster near the diagonal than the one for  $\langle M_{\text{ap}}^2 \rangle$ , and shows a slightly larger correlation at intermediate distances  $x$ . The covariance of  $\langle \mathcal{R}\mathcal{R} \rangle_E$  has been studied in Eifler et al. (2009) and has significantly smaller correlation length than the one for  $\langle M_{\text{ap}}^2 \rangle$ .

### 3.6 Numerical limits on the B-mode $\mathcal{R}_B$

We calculate the B-mode  $\mathcal{R}_B$  from equation (1) by using  $\tilde{T}_-$  obtained from the optimal function  $\tilde{T}_+$  (see Section 2.4). Theoretically,

$\mathcal{R}_B$  vanishes but there could be a residual B mode because the E-/B-mode decomposition might not be perfect. For example, there could be numerical issues regarding the matrix inversion of equation (20). Our values of  $\mathcal{R}_B$  are limited by the precision of the numerical integration of equation (1).  $\mathcal{R}_B$  goes to zero for decreasing integration step size and we did not find evidence for a residual B mode. For a step size of  $\Delta\vartheta = 5 \times 10^{-4}$  arcsec, we find  $\mathcal{R}_B/\mathcal{R}_E < 2 \times 10^{-5}$  for all angular scales. Even if a residual B mode should be present, it is straightforward to make it vanish identically. One can increase the polynomial order  $N$  of the decomposition by one, and determine the corresponding coefficient  $a_{N-1}$  such that  $\mathcal{R}_B = 0$ .

### 3.7 Dependence on cosmology and survey parameters

The results presented in this paper have been obtained by using a specific covariance matrix of  $C_{++}$ , namely the one used in Fu et al. (2008), and by choosing a specific cosmology. Here, we briefly describe how our results change when we modify these parameters.

First, we illustrate the dependence on the covariance matrix. Instead of using the full covariance, as was done in the previous sections, we repeat the S/N analysis by taking the diagonal shot-noise component only. This noise originates from the intrinsic galaxy ellipticity dispersion. As expected, the S/N and FoM increase substantially, mainly because of the missing cross-correlation between angular scales in the shear correlation function. For all three cases,  $\mathcal{R}_E$ ,  $\langle M_{\text{ap}}^2 \rangle$  and  $\langle \mathcal{R}\mathcal{R} \rangle_E$ , the S/N increases monotonously with  $\Psi$  beyond the maximum scale and does not show a peak at around 20 arcmin. The relative trend between the three cases stays the same.

We change the fiducial cosmological model by increasing  $\sigma_8$  from 0.8 to 0.9. This results in an increase of S/N of a factor between 1.3 and 1.4, which is roughly the same for  $\mathcal{R}_E$ ,  $\langle M_{\text{ap}}^2 \rangle$  and  $\langle \mathcal{R}\mathcal{R} \rangle_E$ . Increasing the mean redshift from 0.95 to 1.19 caused the S/N to be higher by 1.8 to 2, in the same way for all three cases. We conclude that the relative difference is not dependent on cosmology or the redshift distribution.

We repeat the calculation of S/N by choosing a fixed  $\vartheta_{\min}$  which is different from our standard value of 0.2 arcmin. The improvement of  $\mathcal{R}_E$  over  $\langle \mathcal{R}\mathcal{R} \rangle_E$  decreases for decreasing  $\vartheta_{\min}$ , by about  $\Delta(\text{S/N}) = 0.1$  for  $\Delta\vartheta_{\min} = 0.1$  arcmin, averaged over all scales  $\Psi$ . This might be because  $\langle \mathcal{R}\mathcal{R} \rangle_E$  shows less cross-correlation between scales which leads to a larger gain when additional scales are included. The gain of  $\mathcal{R}_E$  with respect to  $\langle M_{\text{ap}}^2 \rangle$  increases when lowering  $\vartheta_{\min}$ , as expected, since the inclusion of more small scales boosts the S/N. On average, the difference is 0.05 for each 0.1 arcmin which leads to an asymptotic value of  $[\text{S/N}(\mathcal{R}_E)]/[\text{S/N}(\langle M_{\text{ap}}^2 \rangle)] = 1.31$ .

To check the stability of the results, we add an independent, uniform random variable between  $-p$  and  $p$  to each of the highest  $N - K$  coefficients  $a_n$  after the optimum has been found. For each randomization, we fix  $a_0, \dots, a_{K-1}$  as described in Section 2.3 to assure E-/B-mode separation. The S/N and FoM are very robust against changes in the coefficients. For both  $p = 0.01$  and  $0.1$ , the changes in S/N and FoM are of the order of  $p$  and less.

## 4 SUMMARY

We have introduced a new second-order cosmic shear function which has the ability to separate E and B modes on a finite interval of angular scales. This function is a generalization of the recently introduced ‘ring statistic’ (SK07). Providing the second-order E-/B-mode shear field correlations, general filter functions

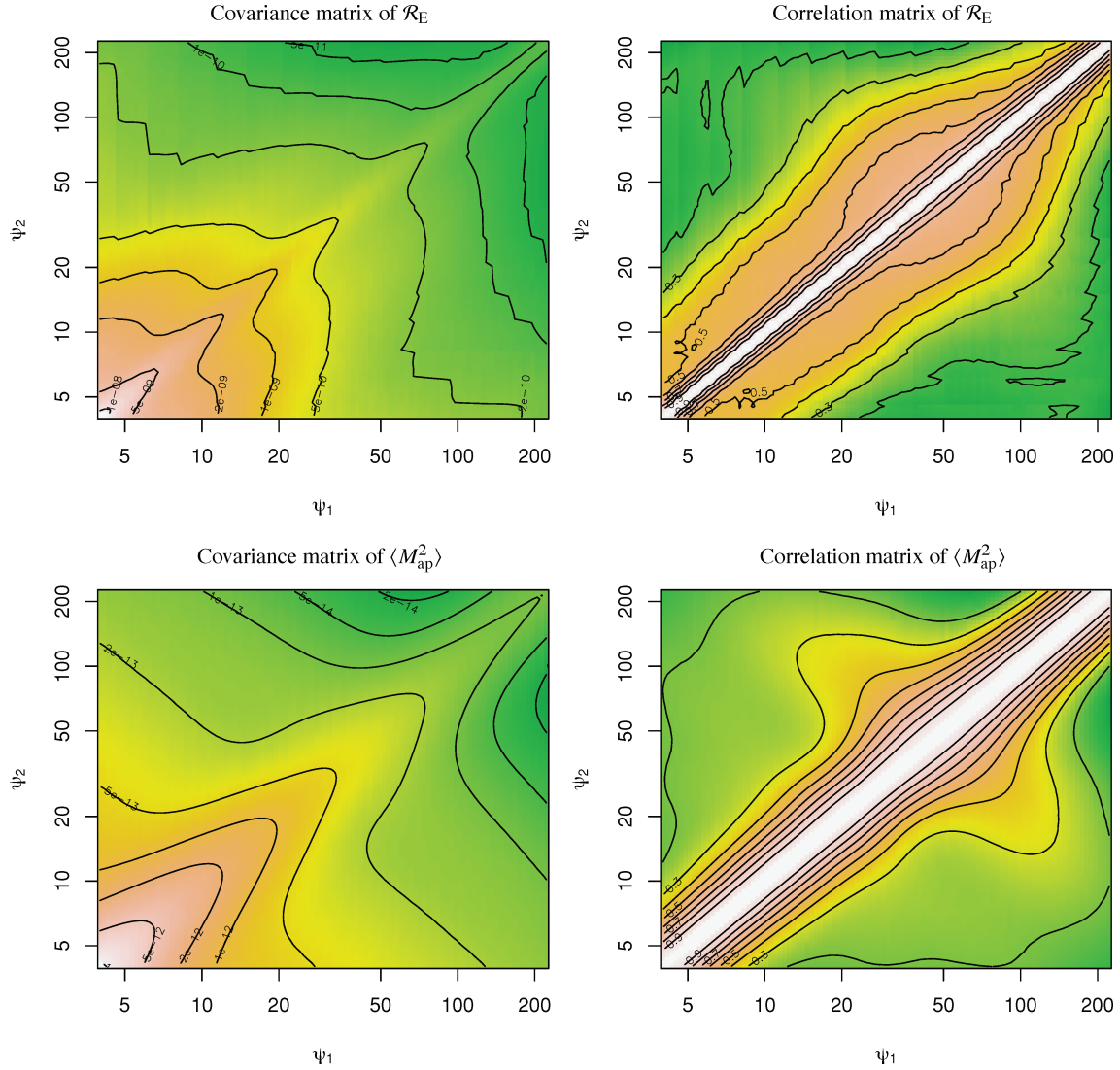


**Figure 6.** Covariance matrix (left-hand panels) and correlation matrix (right-hand panel) of  $\mathcal{R}_E$ , optimized for the FoM (equation 37) with  $\eta = 1/50$  (top), and of the aperture-mass dispersion with  $\Psi_i$  being equal to the aperture diameter (bottom). The colours correspond to the same levels for  $\mathcal{R}_E$  and  $\langle M_{\text{ap}}^2 \rangle$ . In the right-hand panels, the contour lines start from the innermost value of 0.9 and are spaced by 0.1.

are calculated and optimized for a specific goal. In this paper, we considered the S/N as a function of angular scale, and an FoM based on the Fisher matrix of the cosmological parameters  $\Omega_m$  and  $\sigma_8$  as optimization criteria.

Our method to find the optimal filter function consists in the following steps:

- (1) Choose the polynomial of order  $N$  and number of constraints  $K \geq 2$  and define a quantity  $Q$  to be maximized (in this work, the S/N and the Fisher matrix FoM).
- (2) Draw a random starting vector of coefficients  $a_K, \dots, a_{N-1}$ .
- (3) For  $m = 0 \dots K - 1$ , calculate  $s_m$  (equation 19).
- (4) Invert the constraints matrix equation (20) to get the first  $K$  coefficients  $a_0 \dots a_{K-1}$ .
- (5) Compute the filter function  $T_+$  (equations 11 and 14).
- (6) Calculate the shear function  $\mathcal{R}_E$  (equation 7) and  $Q$  (in this work, equations 35 and 36).
- (7) Maximize  $Q$ . At each iteration of the maximization process, repeat steps 3–6.

We were able to improve both S/N and FoM substantially with respect to the SK07 ring statistic. Moreover, we obtained better results than for the aperture-mass dispersion  $\langle M_{\text{ap}}^2 \rangle$ , even though the latter formally extends to zero lag and includes therefore more small-scale power.

We have adapted and optimized our new second-order statistic  $\mathcal{R}_E$  to a specific cosmology and survey parameters such as area and depth. We used a smallest scale of 0.2 arcmin which corresponds to the smallest separation for which galaxy images can easily be separated using ground-based imaging data. The cosmic shear-correlation covariance corresponds to the CFHTLS-Wide third data release used for weak cosmological lensing (Fu et al. 2008). The coefficients corresponding to the optimal filter functions can be found in Table 2. A C-program which calculates the filter functions and the shear statistic  $\mathcal{R}_E$  is freely available.<sup>4</sup>

<sup>4</sup>[http://www2.iap.fr/users/kilbinge/decomp\\_eb/](http://www2.iap.fr/users/kilbinge/decomp_eb/)

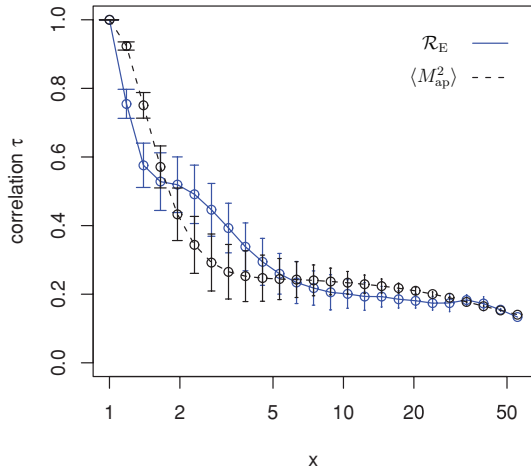


**Figure 7.** The average correlation  $\tau$  (equation 39) for scales which are separated by the ratio  $x$ , for  $\mathcal{R}_E$  (solid, blue lines) and  $\langle M_{\text{ap}}^2 \rangle$  (dashed, black curve). The error bars indicate the scatter when averaging over different scales  $\Psi$ .

Our specific results can be applied to other requirements, although the results will not be optimal. Alternatively, the optimization method described here can easily be applied to any given survey setting. For space-based surveys, where the galaxy-blending confusion limit is smaller than for ground-based observations, the advantage of  $\mathcal{R}_E$  over  $\langle M_{\text{ap}}^2 \rangle$  is more pronounced.

## 5 OUTLOOK

The new cosmic shear functions  $\mathcal{R}_E$  and  $\mathcal{R}_B$  can be applied in various ways in the context of detecting systematics in cosmic shear data and for constraining cosmological parameters.

The optimization for S/N is useful for detecting a potential B mode in the data. In this case, the E/B-mode decomposition serves merely as a diagnostic of the observations. A significant B mode can be a sign for residuals in the PSF correction or non-perfect shape measurement. It might also hint to an astrophysically generated B-mode signal, for example, from shape–shear correlations or shape–shape intrinsic alignment. In both cases, the B-mode signal is expected to be small and it is of great importance to obtain a clear E/B-mode separation without mixing of modes.

In case of a suspected astrophysical B mode, the separation of the shear field into E and B modes might be a decisive advantage. If the power spectrum contains both an E and B mode,  $P_{\text{tot}} = P_E + P_B$ , both modes mix together into their Fourier-transform of  $P_{\text{tot}}$ , the shear correlation function. Thus, the E and B mode may not be uniquely reconstructed from the correlation functions. The different astrophysical components giving rise to  $P_E$  and  $P_B$  can then only be separated by a E/B-mode separating filter.

The FoM optimization permits  $\mathcal{R}_E$  to be used for efficient constraints on cosmological parameters. The reason to use a filtered version of the shear correlation function  $\xi_{\pm}$  instead of the latter directly can be manifold (Eifler, Kilbinger & Schneider 2008). A filter can be chosen to be a narrow passband filter of the power spectrum and is therefore able to probe its local features, unlike the broad low-passband function  $\xi_{+}$ . As a consequence, the correlation length is much smaller and the covariance matrix close to diagonal. This has numerical advantages in particular in the case of many data points, e.g. for shear tomography. Finally, higher-order moments (skewness, kurtosis, etc.) of filtered quantities are eas-

ier to handle than higher-order statistics of the (spin-2) shear field (Jarvis, Bernstein & Jain 2004; Schneider, Kilbinger & Lombardi 2005).

Apart from S/N and FoM maximization, one can think of other, alternative quantities with respect to which the filter function can be optimized. For example, if a model for the B mode is assumed, the S/N of  $\mathcal{R}_B$  can be optimized to facilitate the possible detection of a B mode. Further, if cosmic shear is combined with other probes of cosmology, the relative gain from weak lensing could be maximized. This can be done for specific goals, for example a given dark-energy parametrization or some alternative theory of modified gravity. However, we emphasize that the possibilities are restricted since the optimization is always limited by the information contained in the lensing power spectrum.

In the case of shear tomography, where the shear signal from different redshifts is resolved (although only partially due to the broad lensing efficiency kernel), one can perform a redshift-dependent optimization of the filter function. This is expected to bring further improvements: first, the projection of physical on to angular scales varies with redshift; using a redshift-dependent filter function, physical scales can be sampled optimally with redshift. Secondly, the power spectrum changes with varying redshift; to optimize the sampling of this redshift-dependent information might require a redshift-varying filter.

$\mathcal{R}_E$  is beneficial in particular on small scales, where the aperture-mass dispersion suffers from mode-mixing. On scales less than a few arcmin, there is a leakage of modes of about 10 per cent (Kilbinger et al. 2006). Those scales contain information about halo structure, substructure and baryonic physics. It is difficult to model those effects; the use of those small scales to constrain cosmological parameters is limited. On the other hand, lensing observations on small scales will provide important constraints on the physical processes involved and matter properties on small scales.

## ACKNOWLEDGMENTS

The authors want to thank Peter Schneider for fruitful discussions and helpful comments during all stages of this work. We thank Ismael Tereno, Mario Radovich, Yannick Mellier and Tim Eifler for useful comments of the manuscript. LF acknowledges the support of the European Commission Programme 6th framework, Marie Curie Training and Research Network ‘DUEL’, contract number MRTN-CT-2006-036133. MK is supported by the CNRS ANR ‘ECOSSTAT’, contract number ANR-05-BLAN-0283-04. MK thanks the Osservatorio di Capodimonte in Naples for their hospitality. This project is partly supported by the Chinese National Science Foundation Nos. 10878003 and 10778725, 973 Program No. 2007CB 815402, Shanghai Science Foundations and Leading Academic Discipline Project of Shanghai Normal University (DZL805).

## REFERENCES

- Albrecht A. et al., 2006, Report of the Dark Energy Task Force, preprint (astro-ph/0609591)
- Benjamin J. et al., 2007, MNRAS, 381, 702
- Crittenden R. G., Natarajan P., Pen U.-L., Theuns T., 2002, ApJ, 568, 20
- Eifler T., Kilbinger M., Schneider P., 2008, A&A, 482, 9
- Eifler T., Schneider P., Krause E., 2009, preprint (arXiv:0907.2320)
- Eisenstein D. J., Hu W., 1998, ApJ, 496, 605
- Fu L. et al., 2008, A&A, 479, 9

- Hamilton A. J. S., 2000, MNRAS, 312, 257  
 Heavens A., Réfrégier A., Heymans C., 2000, MNRAS, 319, 649  
 Hetterscheidt M., Simon P., Schirmer M., Hildebrandt H., Schrabback T., Erben T., Schneider P., 2007, A&A, 468, 859  
 Hoekstra H., Jain B., 2008, Annu. Rev. Nuclear Part. Sci., 58, 99  
 Jarvis M., Bernstein G., Jain B., 2004, MNRAS, 352, 338  
 Jarvis M., Jain B., Bernstein G., Dolney D., 2006, ApJ, 644, 71  
 Kaiser N., 1992, ApJ, 388, 272  
 Kilbinger M., Schneider P., 2004, A&A, 413, 465  
 Kilbinger M., Schneider P., Eifler T., 2006, A&A, 457, 15  
 Kilbinger M. et al., 2009, A&A, 497, 677  
 Leauthaud A. et al., 2007, ApJS, 172, 219  
 Mackey J., White M., Kamionkowski M., 2002, MNRAS, 332, 788  
 Massey R. et al., 2007, ApJS, 172, 239  
 Munshi D., Valageas P., Van Waerbeke L., Heavens A., 2008, Phys. Rep., 462, 67  
 Peacock J. A., Schneider P., Efstathiou G., Ellis J. R., Leibundgut B., Lilly S. J., Mellier Y., 2006, Technical report, ESA-ESO Working Group on 'Fundamental Cosmology'. ESA, Noordwijk, preprint (astro-ph/0610906)  
 Press W. H., Teukolsky S. A., Flannery B. P., Vetterling W. T., 1992, Numerical Recipes in C. Cambridge Univ. Press, Cambridge  
 Schneider P., Kochanek C. S., Wambsganss J., 2006, Gravitational Lensing: Strong, Weak and Micro, Saas-Fee Advanced Courses, Vol. 33. Springer-Verlag, Berlin  
 Schneider P., Kilbinger M., 2007, A&A, 462, 841 (SK07)  
 Schneider P., Van Waerbeke L., Mellier Y., 2002, A&A, 389, 729  
 Schneider P., Kilbinger M., Lombardi M., 2005, A&A, 431, 9  
 Schneider P., Van Waerbeke L., Jain B., Kruse G., 1998, MNRAS, 296, 873  
 Schrabback T. et al., 2007, A&A, 468, 823  
 Semboloni E., Van Waerbeke L., Heymans C., Hamana T., Colombi S., White M., Mellier Y., 2007, MNRAS, 375, L6  
 Smith R. E. et al., 2003, MNRAS, 341, 1311

## APPENDIX A: SIMULTANEOUS OPTIMIZATION FOR ARBITRARY SCALES

The optimization scheme introduced in this paper holds for a given ratio of minimum and maximum scale  $\eta = \vartheta_{\min}/\vartheta_{\max}$ . In this section, we introduce a simple generalization of the scheme to obtain an optimized function  $\tilde{T}_+$  which fulfils the integral constraints (equation 9) for all  $(\vartheta_{\min}, \vartheta_{\max})$ . This comes at the expense of a poor resulting S/N.

If we demand the following relation to hold

$$I_\nu \equiv \int_{-1}^{+1} dx x^\nu \tilde{T}_+(x) = 0; \quad \text{for } \nu = 0, 1, 2, 3, \quad (\text{A1})$$

then the two integral constraints

$$RI_0 + I_1 = R^3 I_0 + R^2 I_1 + RI_2 + I_3 = 0 \quad (\text{A2})$$

are satisfied. However, instead of two conditions we have now four equations (equation A1) which fix  $K = 4$  coefficients of the decomposition. In this case, the first four matrix elements are (cf. equation 17)

$$f_{mn} = \int_{-1}^{+1} dx x^m C_n(x); \quad m = 0 \dots 3. \quad (\text{A3})$$

Since there are two more integrals than in the previous case, the resulting function has at least two more zeros. The corresponding S/N is significantly lower than in the single-scale case; it is even smaller than the one obtained for  $Z_+$ . We therefore do not consider this option further.

This paper has been typeset from a  $\text{\TeX}/\text{\LaTeX}$  file prepared by the author.